Geophys. J. Int. (2005) **162,** 882–898

A one–way wave equation for modelling seismic waveform variations due to elastic heterogeneity

D.A. Angus ⋆

Department of Geological Sciences and Geological Engineering, Queen's University, Kingston, ON, Canada K7L 3N6

Submitted to GJI: Spring 2005

SUMMARY

The application of a new one–way narrow–angle elastic wave equation to isotropic heterogeneous media is described. This narrow–angle finite–difference propagator should provide an efficient and accurate method of simulating primary body–wave(s) passing through smoothly–varying heterogeneous media. Although computationally slower than ray theory, the narrow–angle propagator can model frequency–dependent forward diffraction and scattering as well as the averaging effects due to smooth variations in medium parameters that vary on the sub–Fresnel zone level. Example waveforms are presented for the propagation of body–waves in deterministic as well as stochastic heterogeneous three–dimensional Earth models. Extrapolation within deterministic media will highlight various familiar wave–diffraction and pulse–distortion effects associated with large–scale inhomogeneities, such as geometrical spreading, wavefront folding and creeping–wave diffraction by a compact object. Simulation within stochastic media will examine the effects of varying the correlation lengths of random heterogeneities on wave propagation. In particular, wave phenomena such as frequency–dependent forward scattering, the appearance of random caustics and the generation of seismic coda will be shown.

Key words: body waves, heterogeneity, one–way wave equation, finite–differences, seismic waveforms.

1 INTRODUCTION

Heterogeneity in the Earth exists on a variety of scales, ranging from several tens of kilometers to meters in tectonic settings (e.g., Sato & Fehler, 1998) and down to millimeters in hand–sample specimens (e.g., Hollinger et al., 1994; Nishizawa et al., 1997). Depending on the frequency content of the probing seismic energy as well as the geometry and scale–length of inhomogeneities, a heterogeneous medium may appear either very simple (e.g., producing obvious or predictable wave phenomena) or extremely complex (e.g., generating incoherent wavefront and waveform distortion, as well as strong attenuation or scattering of seismic energy). Heterogeneities can lead to focussing and de–focussing of transmitted energy and will not only result in traveltime and amplitude anomalies, but will also result in frequency–dependent waveform or pulse distortions (e.g., Trorey, 1970; Hilterman, 1970; Korneev & Johnson, 1993). When heterogeneities have size on the order of or smaller than the seismic wavelength, diffraction or scattering may result in the appearance of random caustics (e.g., White et al., 1988) and the generation of seismic coda (e.g., Aki, 1969).

Given that large portions of the lithosphere show spatial heterogeneity on several length–scales (e.g., Goff & Hollinger, 1999) in comparison to the seismic signals, the net effect of diffraction and scattering may be difficult to assess. Kravtsov et al. (2003) suggest that a realistic description of wave propagation in heterogeneous media would involve deterministic Earth models supplemented with statistical information regarding the finer–scale randomized inhomogeneities. Therefore, with ongoing improvements in data quality and quantity, it is becoming increasingly important to consider a more complete range of diffraction and scattering regimes when simulating wave propagation in heterogeneous media.

⋆Now at: Department of Physics, New Mexico State University, Las Cruces, NM, USA, 88003-8001

Ray based approaches applied to the modelling of seismic waves are limited to smoothly–varying media, where heterogeneities have length–scales that are larger than the Fresnel zone and the velocity contrasts are small. For increasingly heterogeneous media (i.e., as the scale–length of the inhomogeneities relative to the seismic wavelengths become smaller), ray theory tends to be problematic in part due to the chaotic behaviour of rays (Keers et al., 1997). Furthermore, the frequency–dependent smoothing that takes place during wave propagation is generally beyond the capabilities of standard ray–based techniques and so the resolution of 'finer' scale features on the order of or less than the Fresnel zone (i.e., within the vicinity of the ray) is poor (Snieder, 1999). As well, the degree of multi–pathing even in the pre–chaotic region can be so severe that handling caustics can be difficult (e.g., Witte et al., 1996).

When the medium inhomogeneities introduce significant off–path or off–ray effects, the Born and Rytov approximations have been shown to be effective in various forward modelling applications (e.g., Chapman & Coates, 1994; Müller & Shapiro, 2001; Müller et al., 2002). In scenarios where the data are insufficient for effective application of the Born or Rytov diffraction approach (e.g., teleseismic studies), the ray/Born approach (e.g., Keers et al., 2000) can be applied, where Fréchet kernels are used to describe the off–path or off–ray travel–time sensitivities (e.g., Dahlen et al., 2000). Furthermore, recent improvements in data quality and quantity have allowed application of true waveform rather than frequency–dependent travel–time diffraction methods to teleseismic body–wave studies of the upper–mantle structure (e.g., Bostock & Rondenay, 1999).

Full–waveform modelling methods, such as the finite–difference (e.g., Alterman & Karal, 1968; Kelly et al., 1976), finite–element (e.g., Smith, 1975; Komatitsch & Tromp, 1999) and pseudo–spectral (e.g., Kosloff et al., 1984; Fornberg, 1987) methods, overcome the limitations imposed by the high–frequency ray approximations as well as the weak scattering assumption required by the linearization of the wave solution. Furthermore, full–waveform methods can model the averaging effects due to variations in material properties on the 'sub–Fresnel' zone level. Although full–wave methods provide accurate waveforms for complex geologic models, they still remain computationally prohibitive for large three–dimensional problems, especially when the medium is anisotropic. The one–way or parabolic equation (e.g., Claerbout, 1970; Tappert & Hardin, 1974; Fishmann & McCoy, 1984) and phase–screen (e.g., Wu, 1994; Wild & Hudson, 1998; le Rousseau & de Hoop, 2001) methods attempt to retain some of the more important signals of interest in the calculated solution while reducing the computational expense.

In this paper, the narrow–angle one–way elastic wave equation of Thomson (1999) is applied to a range of heterogeneous isotropic media (for applications to homogeneous anisotropic media see Angus et al., 2004). It should be stressed that the examples presented are by no means revolutionary and are not intended to highlight any new heterogeneous wave phenomena. Rather, they are appropriate benchmarks for the new one–way method. In particular, the frequency–dependent effects of geometrical spreading as well as the forward diffraction and scattering due to various inhomogeneities are studied.

2 THE ONE–WAY WAVE EQUATIONS

The derivations of one–way or parabolic wave equations can be split into two categories; methods that factorize the wave solution (e.g., Claerbout, 1970) and methods that factorize the wave equation (e.g., Fishmann & McCoy, 1985). In both cases, factorization involves choosing a preferred axis or direction of propagation followed by splitting the solution or differential operator into two factors. The reference phase approach (i.e., the factorization of the wave solution) involves a 'localization' of an exact non–local operator and hence is explicitly restricted to narrow angles as well as weak and slowly–varying inhomogeneous media. In contrast, the operator–splitting approach seeks an approximate expression for a 'pseudo–differential operator' (i.e., the square–root of the differential operator) in terms of an asymptotic or 'high–frequency' solution and allows relaxing the restriction of weak lateral inhomogeneity and narrow–angle propagation. Hence, this asymptotic approximation retains some of the global properties of the operator–root and some full–waveform effects are included, at least for the frequency ranges of interest here.

The operator splitting approach is exact for forward propagation when there is no range dependence (i.e., the forward and reverse propagating waves are de–coupled). However, when gradients in the forward–direction become significant, it is possible to account for the coupling between the forward and reverse waves. For instance, de Hoop & de Hoop (1994) introduced a 6×6 'displacement–stress' matrix formulation which has been known to be a convenient approach when dealing with laterally–homogeneous medium boundary–value (or reflection/transmission) problems (e.g., Woodhouse, 1974; Kennett, 1983). In de Hoop & de Hoop (1994), the forward– and reverse–wave coupling is approximated using an iterative process based on a generalization of the Born method (e.g., Chapman, 1981).

Thomson (1999) introduced a hierarchy of one–way wave equations based on a 3×3 matrix factorization of the elastic wave equation for three–dimensional, generally–anisotropic, heterogeneous media. The 3×3 matrix formulation allows parallels to be drawn with familiar (or conventional) ray–based approaches. This formulation can be reduced to a path–integral representation or to the standard ray limit via the stationary–phase approximation (see Thomson, 1999).

This one–way seismic wavefield extrapolator is more generally applicable than ray methods, primarily because it can handle robustly transitions from weak–to–strong or arbitrary anisotropy. Although these wave equations are based on a 3×3

displacement formulation, it is possible to include the coupling between forward and reverse propagating waves (Thomson, submitted).

The explicit integral formulation of the single frequency ω one–way wave equation is (Thomson, 1999)

$$\partial_1 \mathbf{u} = \mathrm{i}\omega \left(\frac{\omega}{2\pi}\right)^2 \int\int \mathbb{P}(x_\alpha, p_\alpha) \exp\left[\mathrm{i}\omega(x_\alpha - y_\alpha)p_\alpha\right] \mathbf{u}(y_\alpha) dy_\alpha dp_\alpha \ , \tag{2.1}$$

where $\mathbf{u}$ is the three–component displacement vector and it is understood that Cartesian coordinates x_i and the summation convention are being used. An alternative and more direct derivation is given by Angus et al. (2004). The propagation direction is taken to be more or less along the x_1 axis and the lateral coordinates $x_{2,3}$ and slownesses $p_{2,3}$ are denoted with Greek subscripts (e.g., x_α and p_α). The ω–independent and (x_α,p_α)–dependent wide–angle propagator is defined by

$$\mathbb{P}(x_\alpha, p_\alpha) = \mathbf{G}\mathbf{P}_1\mathbf{G}^{-1} \tag{2.2}$$

where $\mathbf{P}_1$ and $\mathbf{G}$ are 3×3 plane–wave eigenvalue and eigenvector matrices. The elements of the diagonal matrix $\mathbf{P}_1$ are the x_1–components of slowness of the forward–propagating waves and the columns of $\mathbf{G}$ are given by the corresponding three allowed polarizations or eigendisplacements (Musgrave, 1970; Fryer & Frazer, 1984; Červený, 2001).

This equation can correctly describe the leading–order ray theory, Maslov and Kirchhoff–like representations including rays which range widely over x_α and p_α. More importantly, it describes the coupling between wave modes in media exhibiting not only strong anisotropy but also weak anisotropy. Furthermore, it is capable of modelling coupling in regions near slowness–surface singularities. This is mainly due to the form of the propagator, which is slowly varying even when there are rapid variations of the individual eigenvector columns of $\mathbf{G}$ (see Angus et al., 2004). However, the solution to this equation requires careful sampling of the integrals for accurate numerical evaluation and hence may not be computationally practical for routine use on small desktop computers.

Equation (2.1) is valid for wide angles as the derivation makes no explicit assumptions about p_α being small. For many practical scenarios only a limited range of p_α is needed and so further approximations to equation (2.1) are possible. For narrow angles, an approximation to the propagator matrix $\mathbb{P}$ can be obtained from a Taylor series expansion about p_α of the form

$$\mathbb{P} \approx \mathbf{P}_0 + \mathbf{P}_\alpha p_\alpha + \mathbf{P}_{\alpha\beta} p_\alpha p_\beta \ . \tag{2.3}$$

This narrow–angle approximation should be appropriate when the incident wavefront is near planar or gently curved. The 'subpropagator' matrices $\mathbf{P}_0$, $\mathbf{P}_\alpha$ and $\mathbf{P}_{\alpha\beta}$ are obtained from the following recursive equations (Thomson, 1999)

$$\mathbf{P}_0 = \sqrt{\rho \mathbf{C}_{11}^{-1}}, \tag{2.4}$$

$$\mathbf{P}_0\mathbf{P}_\alpha + \mathbf{P}_\alpha\mathbf{P}_0 = -\mathbf{C}_{11}^{-1}(\mathbf{C}_{1\alpha} + \mathbf{C}_{\alpha 1})\mathbf{P}_0, \tag{2.5}$$

$$\mathbf{P}_0\mathbf{P}_{\alpha\beta} + \mathbf{P}_{\alpha\beta}\mathbf{P}_0 = -\mathbf{C}_{11}^{-1}\mathbf{C}_{\alpha\beta} - \mathbf{C}_{11}^{-1}(\mathbf{C}_{1\alpha} + \mathbf{C}_{\alpha 1})\mathbf{P}_\beta - \mathbf{P}_\alpha\mathbf{P}_\beta. \tag{2.6}$$

The matrix $\mathbf{C}_{11}$ is real and symmetric, and for isotropic media reduces to a diagonal matrix whose elements relate closely to the inverse wavespeeds (Woodhouse, 1974). The eigensolution of $\mathbf{C}_{11}$ must be known to construct the symmetric matrix $\mathbf{P}_0$. The 'higher–order' propagators (2.5) and (2.6) ostensibly require the solution to nine simultaneous equations of a 9×9 matrix constructed from $\mathbf{P}_0$. However, an alternative approach is based on the symmetry properties of $\mathbf{P}_0$. For instance, the difference between equation (2.5) and its transpose leads to three independent equations for the antisymmetric part of $\mathbf{P}_\alpha$. Adding equation (2.5) and its transpose leads to six equations for the symmetric part of $\mathbf{P}_\alpha$.

An intuitive understanding of the subpropagator matrices $\mathbf{P}_0$, $\mathbf{P}_\alpha$ and $\mathbf{P}_{\alpha\beta}$ can be found be inspecting their form in the isotropic limit. The matrix $\mathbf{P}_0$ is diagonal and serves to advance the individual plane–wave modes in the x_1 direction. The matrices $\mathbf{P}_\alpha$ have only off–diagonal elements and are associated with P– to S–wave coupling. The matrices $\mathbf{P}_{\alpha\beta}$ are diagonal when $\alpha = \beta$ and non–diagonal otherwise, and appear to describe the effect of wavefront curvature.

Substitution of the narrow–angle propagator (2.3) into the integral equation (2.1) and noting that $\partial_\alpha \Leftrightarrow \mathrm{i}\omega p_\alpha$ yields the frequency–domain narrow–angle one–way wave equation

$$\partial_1 \mathbf{u} = \mathrm{i}\omega \mathbf{P}_0 \mathbf{u} + \mathbf{P}_\alpha \partial_\alpha \mathbf{u} + \frac{1}{\mathrm{i}\omega} \mathbf{P}_{\alpha\beta} \partial_\alpha \partial_\beta \mathbf{u} \ . \tag{2.7}$$

This frequency domain wave extrapolator has been implemented using simple second–order accurate difference operators for all spatial derivatives. A description of the finite–difference algorithm and subsequent numerical analysis is given in Angus & Thomson (submitted).

3 NUMERICAL EXAMPLES

3.1 Deterministic examples

3.1.1 Low–velocity spherical inclusion

In this first example, the low–velocity sphere is defined by the smooth analytic velocity function

$$v^{\nu}(r) = (v_s^{\nu} - v_0^{\nu})\text{sech}\left(\frac{\pi r_s^3}{720 s_c^3}\right) + v_0^{\nu} \ , \tag{3.1}$$

where the radius r_s is measured from the center of the sphere, s_c is a scaling factor that determines the effective width of the sphere, v_0^{ν} is the reference or background velocity, v_s^{ν} is the velocity at the center of the sphere and ν specifies the wavetype P or S (Raymer, 2000, equation 4.35). The low–velocity sphere is embedded within a homogeneous cube having a side dimension of 1000 m and background P– and S–wave velocities of approximately 4800 and 2730 m/s. The diameter of the sphere is approximately 200 m (i.e., $s_c = 9$) and the minimum P– and S–wave velocities at the center are roughly 4575 and 2600 m/s (i.e., a 5% velocity perturbation). The sphere is located in the middle of the cube (i.e., $x_\alpha = 500$ m) and at a depth of $x_1 = 300$ m. The incident wave for the examples is of the P type.

The lateral Cartesian grid is defined by 49×49 node points with spacing $\Delta x_\alpha = 5$ m and the forward extrapolation step is $\Delta x_1 = 0.05$ m. The source pulse is a Ricker wavelet sampled $N_t = 128$ times with time increment $\Delta t = 0.25$ ms. For a background isotropic P–wave velocity of 4800 m/s, the incident waveform has a spatial pulse–width of approximately 22 m. Thus, the spherical inhomogeneity has a length–scale about one order of magnitude larger than the spatial pulse width.

Figure 1 displays a representative two–dimensional slice of the normal–incidence rays (i.e., in the x_1–direction) in this velocity model. The rays travelling through the sphere are immediately focussed and this results in the 'conical–shaped' caustic appearing at a depth of approximately 700 m; in three–dimensions, this conical–shaped caustic is a pencil–point cusp. In Figure 2, x_1–component waveforms are displayed for x_2–profiles at x_1–planes of 800, 900 and 1000 m depth. In these plots, time increases from right to left, allowing the later arriving diffraction signals to be visible. The enhanced amplitudes, where the rays cross, are visible among the central receivers and the diffraction or triplication due to the caustic can be seen to spread out laterally from the grid center. The diffraction signal can be seen to trail behind the relatively undisturbed early arrival for the profile at $x_3 = 400$ m and depth $x_1 = 1000$ m. The amplitudes of each panel plot in this particular example have been normalized to the maximum amplitude of the x_2–profile at $x_3 = 500$ m for each x_1–plane and this was done to highlight the three–dimensional variation in amplitudes in the lateral directions.

3.1.2 High–velocity spherical inclusion

The next simulation examines the effect of a high–velocity sphere on an incident plane P–wave. The heterogeneous model is defined by a volume with a lateral x_α dimension of 4000 m, an x_1 depth extent of 2000 m and homogeneous background P– and S–wave velocities of 4575 m/s and 2600 m/s. The high–velocity sphere is defined by equation (3.1) and has a diameter of approximately 500 m (i.e., $s_c = 36$). The center of the sphere is located in the middle of the volume (i.e., $x_\alpha = 2000$ m) and at a depth of $x_1 = 1000$ m. The maximum P– and S–wave velocities at the center of the sphere are approximately 5030 m/s and 2860 m/s (i.e., a 10% velocity perturbation). The source pulse is a Ricker wavelet sampled $N_t = 128$ times with time increment $\Delta t = 0.5$ ms. For a background isotropic P–wave velocity of 4575 m/s, the waveform has a spatial pulse–width of approximately 35 m. Thus, the spherical inhomogeneity has a length–scale several orders of magnitude larger than the spatial pulse–width. The incident wave for the examples is of P type.

Figure 3 displays a two–dimensional section of rays traced in the true velocity model for an incident plane P–wave. In this figure, there are two regions where the rays cross and they form 'funnel–shaped' caustics; in three–dimensions, the caustics would appear as a ring or circular cusp. Also apparent is the geometrical spreading of the rays within the central region.

The Cartesian lateral grid is defined by 41×41 node points with spacing $\Delta x_\alpha = 30$ m and the forward extrapolation step is $\Delta x_1 = 0.125$ m. The lateral grid is centered over the high–velocity sphere and the initial x_1–plane is located at a depth of 400 m. In Figure 4, x_1–component waveforms are plotted for profiles along the x_2–direction at the initial $x_1 = 400$ m plane and two planes at $x_1 = 1500$ m and 2000 m. The reduced amplitude of the central traces are apparent and result from geometrical spreading or de–focussing of the wavefield. Also visible are two shoulders of enhanced amplitudes followed by diffraction signals, which result from focussing within the region mapped out by the ring–cusp triplications due to crossing rays displayed in Figure 3.

In Figure 5, x_1–component waveforms for all three x_2–sections at a depth of 2000 m are plotted. The geometrical spreading is most severe for the portion of the wavefield travelling through the center of the sphere and least for the portion travelling on the shoulder. This figure also highlights an interesting arrival that appears on the central traces; a secondary arrival on the x_2–section at the $x_3 = 1970$ m line having a noticeably lower frequency content (i.e., the region within the dashed ellipse). This signal is believed to result from the portion of the wavefield that 'creeps' or skirts around the edge of the high–velocity

sphere. On the x_2–section at $x_3 = 1820$ m, the low–frequency and low–amplitude creeping diffraction is barely visible and is overshadowed by the ring diffractions coming from the out–of–plane direction (i.e., the region within the dotted ellipse). This creeping phenomenon will be referred to as 'creeping–wave' diffraction and will be discussed below.

3.1.3 Creeping–wave diffraction

The next three simulations study the creeping–wave diffraction signal. The geometry of the model and extrapolation parameters are identical to the low–velocity sphere example and the reference or background P– and S–wave velocities are 4575 m/s and 2600 m/s. For the three simulations, the maximum P– and S–wave velocities at the center of the high–velocity sphere are perturbed by +5%, +6% and +10% of the background velocities. Figure 6 is a sketch of three expected arrivals for a plane–wave incident on a high–velocity sphere; the undisturbed portion of the wavefield, the de–focussed transmitted wavefield and the portion of the wavefield that creeps along the sides of the high–velocity sphere. Increasing the velocity of the sphere will lead to an increase in geometrical spreading (i.e., a decrease in primary waveform amplitudes) as well as a decrease in the propagation time of the de–focussed or transmitted signal. Since the creeping diffraction travels predominantly within the reference medium, it is expected that increasing the velocity of the sphere will yield a larger time separation between the de–focussed and diffracted signals.

In Figure 7, the x_1–component waveforms for all three velocity perturbations are compared for x_2–profiles at a depth of $x_1 = 1000$ m. For the high–velocity sphere with 5% velocity perturbation, the creeping diffraction signal is just slightly behind the earlier reduced–amplitude arrival. For a 6% velocity perturbation, the reduced–amplitude signal arrives just slightly earlier than that of the 5% perturbation and the time delay between the reduced–amplitude and creeping diffraction signal increases. For a 10% velocity pertubation, the time delay between the two signals increases still further and the amplitude of the earlier arrival is significantly reduced due to the greater geometrical spreading. In fact, it appears that the creeping–wave diffraction has 'healed' the initial planar wavefront.

3.2 Caustic examples

In this example, the formation of caustics is investigated using the one–dimensional velocity function given by

$$v^{\nu} = v_0^{\nu} \left[1 + \sqrt{2}\varepsilon \sin\left(\frac{x_\alpha^4}{k} \right) \right] \ , \tag{3.2}$$

where v^{ν} is the x_α–dependent P–wave velocity, $v_0^{\nu} = 4575.5$ m/s is the reference or background velocity, $\varepsilon = 0.035$ is the rms value of velocity fluctuation and $k = 1.44 \times 10^9$ m^4. This one–dimensional velocity field is a modification of the one–dimensional medium with slowness perturbation described by Spetzler & Snieder (2001). The oscillating velocity field described by equation (3.2) for $x_\alpha = x_2$ is displayed in Figure 8 (a). The wavefield is evaluated in Cartesian coordinates on a lateral grid defined by 99×99 node points with lateral spacing $\Delta x_\alpha = 5$ m and the forward propagation step is $\Delta x_1 = 0.025$ m. The source pulse is a Ricker wavelet sampled $N_t = 128$ times with time increment $\Delta t = 0.25$ ms. For a plane P–wave and a reference velocity of 4575 m/s, a total propagation distance of 200 m corresponds to approximately 20 spatial pulse–widths.

For plane–wave initial conditions and a one–dimensional velocity model ($x_\alpha = x_2$ only), the point where caustics begin to form can be predicted by

$$\breve{x}_1(x_\alpha) = \sqrt{\frac{-2}{\frac{\partial^2}{\partial x_\alpha^2}\left(\frac{p(x_\alpha)}{p_0(x_\alpha)} \right)}} \ , \tag{3.3}$$

where the focal distance $\breve{x}_1(x_\alpha)$ is a function of the offset x_α, $p(x_\alpha)$ is the one–dimensional slowness perturbation and $p_0(x_\alpha)$ is the reference or background slowness (Spetzler & Snieder, 2001, equation 11). The focal distance (3.3) for the one–dimensional velocity field defined by equation (3.2) is plotted in Figure 8 (b). Six caustics are predicted to develop over the total propagation distance of 200 m in the x_1–direction. The locations of these predicted caustics are represented by the minima; three early on at an x_1 distance of approximately 25 m, two at 40 and 50 m and the last at 90 m. It should be noted that the one–dimensional velocity field and focal distance are sampled sparsely for lateral grid locations beyond 400 m. Application of the narrow–angle wave equation within this severely oscillatory region is expected to be close to or beyond the limitations of the propagator.

In Figure 9, the evolution of the x_1–component waveforms for an incident plane P–wave are displayed at increments of 20 m (or approximately every spatial pulse–width). At $x_1 = 20$ m, the three predicted caustics are beginning to develop and are clearly visible by the enhanced waveform amplitudes at $x_1 = 40$ m (or points indicated by the lines numbered 1 through 3). The fourth predicted caustic begins to form at $x_1 = 40$ m at approximately $x_2 = 400$ m and is indicated by line 4. Between x_1 =40 and 60 m, the fifth caustic forms and is visible on the $x_1 = 60$ m panel plot near $x_2 = 350$ m (i.e., line 5). Finally, the last caustic begins to form between x_1 =80 and 100 m as indicated by line 6. As predicted by equation (3.3), no other caustics begin to form beyond $x_1 = 100$ m, where the wavefront folding becomes increasingly chaotic at large x_2.

3.3 Random examples

Seismological studies of small–scale heterogeneities generally involve approximating inhomogeneous media with a random distribution. Three random distributions are often considered; these are defined by the Gaussian, exponential and von Kármán spatial autocorrelation functions (ACFs). The Gaussian ACF is better suited to model smooth media than the exponential ACF and this is because the Gaussian function is infinitely differentiable, whereas the exponential function is piecewise continuous and contains first–order discontinuities (van der Baan, 2001). The von Kármán function can describe media that are smoother than the exponential ACF as well as media that have discontinuities on all length–scales (Tatarskii, 1961; van der Baan, 2001). Media that are discontinuous on all length–scales display fractal characteristics and are referred to as being self–similar (Fisk et al., 1992). Since a medium displaying fractal characteristics is beyond the limitations of the narrow–angle wave equation, only the Gaussian and exponential type ACFs will be considered. A range of correlation lengths will be investigated and this will allow characterization of various types of forward diffraction and scattering phenomena (e.g., wave effects due to 'deterministic' regimes characterized by large–scale anomalies down to 'pre–chaotic' regimes characterized by small–scale anomalies). It is important to note that although random media are not intended to model any particular portion of the Earth's interior, they are reasonable models of small–scale structure (Klimeš, 2002). The objective here is to compare qualitatively the likeness of the observed wave effects due to random heterogeneities with previously published results, since no attempt has been made to compare the narrow–angle simulations with an exact reference solution.

3.3.1 'Mantle in a box'

The specific examples considered in this section are referred to as the 'mantle in a box' random heterogeneity models and are the elastic equivalent of the acoustic models given by Baig et al. (2003). In these examples, the velocity field is defined by a statistically homogeneous and isotropic random function and so no shape–induced anisotropy is introduced by the random heterogeneities. The model is defined in the wavenumber–domain, $\mathbf{k} = (k_1, k_2, k_3)$, for a cube having side dimension 1000 m and grid defined by $N^3 = 256^3$ node points with inter–node spacing $\Delta x \approx 4$ m. The amplitude of the dimensionless random field $\hat{c}(\mathbf{k})$ is specified by the square–root of the Gaussian

$$\Phi^{\mathrm{g}}(k) = \epsilon^2 a^3 \exp\left[\frac{-k^2 a^2}{4}\right] \tag{3.4}$$

or exponential

$$\Phi^{\mathrm{e}}(k) = \frac{\epsilon^2 a^3}{(1 + a^2 k^2)^2} \tag{3.5}$$

power spectral density function (PSDF), where a is the correlation length and ϵ is the mean fractional fluctuation. The phases are calculated randomly over a uniform distribution in the interval $[0, 2\pi]$. The random field in the wavenumber–domain is then Fourier transformed into the space–domain $\mathbf{x}$. The homogeneous isotropic reference medium has P– and S–wave velocities of 4575 m/s and 2603 m/s, and a constant density of $\rho = 2160$ kg/m^3. The random P– and S–wave velocity fields are obtained by multiplying the dimensionless random field $\hat{c}(\mathbf{x})$ with the reference medium values. Thus, the P– and S–wave velocity fields share the same random sequence and only differ in terms of magnitude.

A total of eight correlation lengths are considered for both the Gaussian and exponential distributions and they range in size between $a = 500$ m and 4 m (see Table 1). Figure 10 is a graphical representation of the Gaussian and exponential random models for a cube having a side dimension of 1000 m and a correlation length of approximately 8 m (modified from Baig et al., 2003). For all sixteen realizations, the media were limited to very–weak heterogeneity by setting $\epsilon = 1\%$. Furthermore, the random phases were evaluated using a computer random–number generator, where the random sequence was initiated with the same arbitrary value so that the same random sequence was generated for all realizations (Press et al., 1992). In other words, all sixteen realizations represent a 'close' family of random media, where, for example, the Gaussian model with correlation length $a = 500$ m could be considered a very–smooth version of the exponential model with correlation length $a = 4$ m.

For all simulations, plane P– and S–waves were propagated within the random medium having Cartesian grid defined by 49×49 node points with lateral spacing $\Delta x_\alpha = 5$ m and a forward extrapolation step of $\Delta x_1 = 0.05$ m. The Cartesian grid has a lateral dimension of 240 m × 240 m, a depth extent of 1000 m and so represents a subvolume of the initial elastic random model. The elastic constants of the subvolume are obtained by interpolating the initial model onto the Cartesian grid, using the FORTRAN subroutines of FITPACK (Cline, 1981). For the interpolation, only the 'regular' cubic splines are applied. The mean velocities for each realization in the local volume are given in Table 1. It should be noted that the particular dimensions of the model are not consistent with global tectonic scenarios, but rather exploration seismology scenarios. However, the particular dimensions and frequencies can be scaled to match those of global seismology applications (e.g., Angus et al., 2004).

The source pulse is a Ricker wavelet sampled $N_t = 128$ times with time increment $\Delta t = 0.25$ ms. For a background P–

and S–wave velocity of 4275 m/s and 2270 m/s, the P– and S–waves have spatial pulse–widths of approximately 20 m and 10 m, respectively. For a total propagation distance of 1000 m, the P– and S–waves travel approximately 50 and 100 spatial pulse–widths. Wave propagation is in the x_1–direction, where the S–wave displacement is defined to be in the x_2–direction.

Figures 11 and 12 display the x_1–component of the incident plane P–wave and the x_2–component incident plane S–wave waveforms after propagating 1000 m through the Gaussian random media. For most of the correlation lengths considered, the resulting wavefronts and waveforms are distinctly different. Thus, the eight realizations represent a broad range of length–scales for the Gaussian random media for the waveform frequencies of interest. In Figure 11, the wavefront is mildly curved and the waveforms are relatively unmodified for correlation lengths $a = 500$ m and 250 m. At $a = 125$ m and 60 m, the effects of a random caustic are apparent from the enhanced waveform amplitudes within the central region. Below the correlation length of $a = 60$ m, the effects of scattering become successively stronger, where the waveforms are increasingly modified. For the correlation length $a = 4$ m, the wavefront is near–planar and the primary waveforms are only slightly modified, but there is significant scattering. In Figure 12, the characteristics of S–wave scattering for correlation lengths above $a = 32$ m are analogous to those of the P–wave, although the effects of the random caustic appear more pronounced. For correlation lengths below $a = 32$ m, the scattering increases significantly, where the wavefront becomes progressively more incoherent and the waveforms more distorted. This is expected because the S–wave travels a greater distance with respect to its spatial pulse–width than does the P–wave and so the energy is more highly scattered.

Figures 13 and 14 display the x_1–component of the incident plane P–wave and the x_2–component incident plane S–wave waveforms after propagating 1000 m through the exponential random media. For both the P– and S–wave propagation in the exponential media, the effects of the high–wavenumber or smaller–scale scatterers are immediately apparent, even for the correlation length $a = 500$ m. These small–scale scatterers tend to obscure the influence of the low–wavenumber or larger–scale heterogeneities. For instance, the enhanced waveform amplitudes due to the random caustic discussed in the previous figures are also visible in Figures 13 and 14 for the large correlation lengths, although they are not as prominent. As the correlation length becomes smaller, the enhanced amplitudes appear to be increasingly overshadowed by the smaller–scale scatterers. In Figure 14 below the correlation length $a = 32$ m, the wavefront is incoherent and a significant amount of the S–wave energy appears to be multiply–scattered (i.e., transferred to the coda).

The appearance of the random caustic or anomalously large amplitudes in these examples may seem counter–intuitive in media displaying very–weak heterogeneity (i.e., $\epsilon = 0.01$), where the P– and S–wave velocities do not exceed $\pm 4\%$ of the reference or background velocities. Such anomalously large amplitudes have also been observed in reflection seismic data (White et al., 1988), where the enhanced amplitudes can be as large as a factor of two times greater than the mean amplitude, with virtually no observable anomalous traveltimes. White et al. (1988) give an explanation for this phenomenon using the theory of the 'stochastic caustic', where the appearance of random caustics is attributable to small random fluctuations in the Earth's material properties. In fact, the occurrence of random caustics is typical of wave propagation through smooth and weak random inhomogeneities when the length–scale of the heterogeneities is large compared to the seismic wavelength, yet small compared to the total propagation distance (e.g., over several tens of wavelengths or spatial pulse–widths).

Figures 15 and 16 compare the x_2–component waveforms for a plane S–wave in the Gaussian correlated random medium and those in a homogeneous equivalent (i.e., homogeneous medium defined by the mean P– and S–wave velocities of the corresponding random medium) at a propagation distance of $x_1 = 1000$ m. The enhanced waveform amplitudes among the central receivers due to the random caustic are visible for correlation lengths $a = 125$ and 60 m. In Figure 15, it is interesting to note that the enhanced amplitude signals arrive later and the lower–amplitude signals arrive earlier than the reference wavefront (i.e., the plane–wave propagating in the homogeneous medium). This is consistent with the seismic traveltime study of Müller et al. (1992), who observe that early arrivals are connected with low amplitude signals and later arrivals with strong amplitude signals. For correlation lengths $a = 32$ and 16 m, the particular regions of enhanced waveform amplitudes appear to be diminishing in spatial extent, whereas other portions of the wavefront display increasing waveform amplitudes. These enhanced waveform amplitudes likely result from an increase in small–scale scattering, since the wavefront is becoming less and less coherent. Also note that with decreasing correlation length the fluctuations of the first arrival times also decrease. Furthermore, as the correlation length is decreased, the match between the first arrival traveltimes of the S–wave propagating in the random media and those of the S–wave propagating in the mean homogeneous media improves dramatically. This is consistent with the numerical results of Müller et al. (1992) as well as the laboratory ultrasonic and numerical modelling study by Spetzler et al. (2002).

3.3.2 A thin slab of random material in a homogeneous medium

Subduction zones represent structurally complex regions of the Earth's upper mantle and these regions are characterized by strong variations in seismic velocities due to textural, compositional and thermal variations between the subducted slab and the surrounding mantle (Kearey & Vine, 1990). An interesting experiment to consider is the wave propagation effects associated with a thin slab of heterogeneous material within a homogeneous reference medium. This scenario could represent a simplified model of subducted oceanic lithosphere within the upper–mantle, where the oceanic and continental lithosphere are

in thermal equilibrium. The only distinguishing feature between the two regions is a random heterogeneous fabric associated with oceanic crust. Of particular interest would be the effect of this random heterogeneous region on wave propagation along the slab dip direction. In the following simulations, the effect of a random heterogeneous slab embedded within a homogeneous background model is investigated. The background or mantle velocity is the mean velocity of the random heterogeneous slab and so only the effects of the random scattering are significant.

For all examples, the Cartesian grid is defined by 49×49 node points with a lateral spacing of $\Delta x_\alpha = 5$ m and a forward extrapolation step of $\Delta x_1 = 0.05$ m. A total of twelve models are examined and all have a lateral dimension of 240 m $\times$ 240 m and a depth extent of 1000 m. The spatial dimensions and frequencies of the particular subducted slab model are not consistent with upper–mantle scenarios, but can be scaled to match that of global seismology applications. The elastic constants for each model are based on the corresponding 'mantle in a box' Cartesian models having the same correlation length. However, only a representative strip or slab of the random heterogeneous medium of width w in the x_2–direction is used. The remaining volume is defined by the mean P– and S–wave velocities given in Table 1. The width of the slab ranges between 120 m and 5 m and only three correlation lengths of the exponential media are considered ($a \approx 60$, 16 and 4 m). Figure 17 is a qualitative representation of the subducted slab model of width w.

The source pulse is a Ricker wavelet sampled $N_t = 128$ times with time increment $\Delta t = 0.25$ ms. For a background P– and S–wave velocity of 4575 m/s and 2603 m/s, the P– and S–waves have spatial pulse–widths of approximately 22 m and 12 m, respectively. For a total propagation distance of 1000 m, the P– and S–waves travel approximately 40 and 80 spatial pulse–widths. The total S–wave displacement is chosen to be dominantly along the x_2–direction.

Figures 18–20 display the x_2–component waveforms for an incident plane S–wave after propagating a distance of 1000 m through the slab models. For a correlation length $a = 62.5$ m, the wavefront in Figure 18 becomes less coherent along the edges of the lateral grid as the width of the slab increases. As well, the effects of the large–scale heterogeneities on the waveforms among the central receivers also become more pronounced. Edge diffractions due to the variable velocity contrast along the slab boundary are also visible for slab widths of $w = 20$ and 5 m, where the wavefront outside the slab is being continuously refracted or diffracted into and out of the heterogeneous slab. In Figure 19, the scattering effects of the slab having correlation length $a = 16$ m are very similar to those for $a = 62.5$ m, although the edge diffractions are less pronounced. This is because the velocities of the smaller–scale heterogeneities along the slab boundary better match, on average, the homogeneous background velocities. The effects of the smaller–scale heterogeneities for the slab having correlation length $a = 4$ m, shown in Figure 20, are more pronounced. However, the wavefront is more coherent for all slab widths and, in fact, does not appear to be modified at all for slab widths of $w = 20$ and 5 m. In all these examples, the continuous wavefront leakage or transfer into and out of the heterogeneous slab represents a constant source of seismic energy for scattering. A greater understanding of this phenomenon may be helpful in unraveling the finer–scale subduction–zone tectonics (e.g., Furumura & Kennett, 2004).

For the particular frequencies used in these simulations (i.e., period of 5 ms or frequency of 200 Hz), the presence of the heterogeneous slab is visible for the models having correlation lengths of $a = 62.5$ and 16 m for all slab widths. For the model with correlation length $a = 4$ m, the presence of a heterogeneous body is apparent, although the effects are significantly weakened as the width of the slab decreases. For a random medium characterized by relatively small–scale heterogeneities with respect to the seismic wavelength and for relatively large propagation distances (e.g., on the order of several tens of wavelengths), this indicates that the heterogeneous body would need to be much more extensive in size than an equivalent heterogeneous body characterized by relatively large scatterers (i.e., on the order of or larger than the seismic wavelength) in order to be visible.

4 DISCUSSION

The above numerical simulations indicate that the narrow–angle wave equation can produce qualitatively realistic waveforms for various types of heterogeneous isotropic medium. The three–dimensional ring–caustic of the high–velocity sphere and pencil–point caustic of the low–velocity sphere lead to the expected enhanced waveform amplitudes and the later arriving diffractive signals. Furthermore, it is satisfying that the creeping–wave diffraction along the edge of the high–velocity sphere could be simulated. It is also encouraging that caustic formation for a plane–wave in the one–dimensional oscillating velocity field could be predicted, especially in regions where the velocity field is extremely variable. The results from the random heterogeneous examples are also qualitatively consistent with various published results. In particular, the appearance of the enhanced waveform amplitudes due to the formation of random caustics are observed for models where the relative length–scales of the inhomogeneities are large compared to the seismic wavelength.

Although not required by the narrow–angle equation, the random heterogeneous models presented in this chapter were taken to be isotropic. Most studies of wave propagation in so–called random *anisotropic* media, in fact, investigate the effects of inclusion–shape induced anisotropy (e.g., Wu & Aki, 1985; Gibson & Ben–Menahem, 1991; Kravtsov et al., 2003; Müller & Shapiro, 2003), rather than random orientations of underlying intrinsically anisotropic single–crystal elasticities. For inclusion–shape induced random anisotropy, the heterogeneous velocity field is no longer described by a spatially isotropic

correlation function, but rather a spatially anisotropic correlation function. Inclusion–shape induced random anisotropic media are particularly useful in characterizing media displaying preferentially–aligned cracks or fluid inclusions.

Regions of the Earth that have undergone plastic deformation may display an overall texture and preferred crystal orientation and this orientation will be most coherent in regions of greatest coherent deformation and incoherent or random in regions of weakest or no deformation. For example, faulting, slumping and failure of semi–competent rock around salt deposits can lead to salt flows that display complex structures. The deformation process leading to the subsequent salt–dome structures can produce zones of strong simple– and axial–shearing and generate polycrystalline assemblages that display texture as well as preferred crystal alignment (e.g., Raymer et al., 2000). These regions of texture and preferred anisotropic crystal alignment will likely have quasi–random orientations that have the potential of generating interesting anisotropic random heterogeneous wave phenomena, that as yet are unexplored.

The heterogeneous examples presented above demonstrate the narrow–angle vector–wave approach for various deterministic and stochastic media, where the length–scales of the heterogeneities span several orders of size relative to the seismic wavelength. For a narrow range of propagation, the 15° wave equation is an efficient tool for simulating elastic waves for an assortment of three–dimensional seismic diffraction and scattering problems and is capable of incorporating the frequency–dependent effects of wave propagation due to smooth variations in the medium down to the sub–Fresnel scale. Given the local nature of the narrow–angle propagator and its computational efficiency, it has the potential of being a useful tool in the study of more complicated three–dimensional Earth structure of present interest.

ACKNOWLEDGMENTS

Colin Thomson and Gerhard Pratt are thanked for the many fruitful discussions during the course of this work. Tobias Müller and an anonymous reviewer are thanked for helpful comments. Adam Baig is gratefully acknowledged for providing access to the 'mantle in the box' model algorithms. This work was supported by scholarships from the Canadian Society of Exploration Geophysicists and Queen's University as well as a grant from Imperial Oil (Canada) and NSERC Individual Research grants to Colin Thomson.

References

Aki, K., 1969, Analysis of seismic coda of local earthquakes as scattered waves, *J. geophys. Res.,* **74**, 615–631.

Alterman, Z., & Karal, F.C., 1968, Propagation of elastic waves in layered media by finite difference methods, *Bull. seism. Soc. Am.,* **58**, 367–398.

Angus, D. A., Thomson, C. J. & Pratt, R. G., 2004, A one–way wave equation for modelling seismic waveform variations due to elastic anisotropy, *Geophys. J. Int.,* **156**, 595–614.

Angus, D. A. & Thomson, C. J., in prep., Finite–difference implementation of a new narrow–angle one–way anisotropic elastic wave equation, *Geophysics,* submitted.

Baig, A. M., Dahlen, F. A., & Hung, S.– H., 2003, Traveltimes of waves in three–dimensional random media, *Geophys. J. Int.,* **153**, 467–482.

Bostock, M. G., & Rondenay, S., 1999, Migration of scattered teleseismic body waves, *Geophys. J. Int.,* **137**, 732–746.

Červený, V., 2001, *Seismic Ray Theory*, Cambridge University Press.

Chapman, C. H., 1981, Long–period corrections to body waves: Theory, *Geophys. J. R. astr. Soc.,* **64**, 321–372.

Chapman, C. H., & Coates, R. T., 1994, Generalized Born scattering in anisotropic media, *Wave Motion*, **19**, 309–341.

Claerbout, J. F., 1970, Coarse grid calculations of wave in inhomogeneous media with application to delineation of complicated seismic structure, *Geophysics,* **35**, 407–418.

Cline, A. K., 1981, FITPACK-Software package for curve and surface fitting employing splines under tension, Dept. of Comput. Sci. Univ. of Texas at Austin.

Dahlen, F. A., Hung, S.–H. & Nolet, G., 2000, Fréchet kernels for finite–frequency traveltimes – I. Theory, *Geophys. J. Int.,* **141**, 157–174.

de Hoop, M. V., & de Hoop, A. T., 1994, Elastic wave up/down decomposition in inhomogeneous and anisotropic media: an operator approach and its approximations, *Wave Motion*, **20**, 57–82.

Dziewonski, A. M., & Woodhouse, J. H., 1987, Global images of the Earth's interior, *Science*, **325**, 678–683.

Fishmann, L., & McCoy, J. J., 1984, Derivation and application of extended parabolic wave theories. I. The factorized Helmholtz equation, *J. Math. Phys.*, **25**, 285–296.

Fishmann, L., & McCoy, J. J., 1985, A new class of propagation models based on a factorization of the Helmholtz equation, *Geophys. J. R. astr. Soc.,* **80**, 439–461.

Fisk, M. D., Charrette, E. E., & McCartor, G. D., 1992, A comparison of phase screen and finite difference calculations for elastic waves in random media, *J. geophys. Res.,* **97**, 12409–12423.

Fornberg, B., 1987, The pseudospectral method: Comparison with finite differences for the elastic wave equation, *Geophysics,* **52**, 483–501.

Fryer, G. J. & Frazer, L. N., 1984, Seismic waves in stratified anisotropic media, *Geophys. J. R. astr. Soc.,* **78**, 691–710.

Furumura, T. & Kennett, B. L. N., 2004, Guided waves in subduction zones and the heterogeneity structure of the subducted plate, *A.G.U.*, San Francisco, U.S.A..

Gibson, R. L., & Ben–Menahem, A., 1991, Elastic wave scattering by anisotropic obstacles: application to fractured volumes, *J. geophys. Res.,* **96**, 19905–19924.
Goff, J. A., & Hollinger, K., 1999, Nature and origin of upper crustal seismic velocity fluctuations and associated scaling properties: Combined stochastic analyses of KTB velocity and lithology logs, *J. geophys. Res.,* **104**, 13169–13182.
Hilterman, F. J., 1970, Three–dimensional seismic modeling, *Geophysics,* **35**, 1020–1037.
Holliger, K., Levander, A. R., Carbonell, R., & Hobbs, R. W., 1994, Some attributes of wavefields scattered from Ivrea–type lower crust, *Tectonophysics*, **232**, 267–279.
Kearey, P. & Vine, F. J., 1990, *Global Tectonics*, Blackwell Scientific Publications.
Keers, H., Dahlen, F. A., & Nolet, G., 1997, Chaotic ray behaviour in regional seismology, *Geophys. J. Int.,* **131**, 361–380.
Keers, H., Johnson, L. R., & Vasco, D. W., 2000, Acoustic crosswell imaging using asymptotic waveforms, *Geophysics,* **65**, 1569–1582.
Kelly, K. R., Ward, R. W., Treitel, S. & Alford, R. M., 1976, Synthetic seismograms: a finite–difference approach, *Geophysics,* **41**, 2–27.
Kennett, B. L. N., 1983, *Seismic Wave Propagation in Stratified Media*, Cambridge University Press.
Klimeš, L., 2002, Correlation functions of random media, *Pure appl. Geophys.*,**159**, 1811–1831.
Komatitsch, D. & Tromp, J., 1999, Introduction to the spectral–element method for 3–D seismic wave propagation, *Geophys. J. Int.,* **139**, 806–822.
Korneev, V. A., & Johnson, L. R., 1993, Scattering of elastic waves by a spherical inclusion – I. Theory and numerical results, *Geophys. J. Int.,* **115**, 230–250.
Kosloff, D., Reshef, R. & Loewenthal, D., 1984, Elastic wave calculations by the Fourier method, *Bull. seism. Soc. Am.,* **74**, 875–891.
Kravtsov, Y. A., Muller, T. M., Shapiro, S. A., & Buske, S., 2003, Statistical properties of reflection traveltimes in 3–D randomly inhomogeneous and anisomeric media, *Geophys. J. Int.,* **154**, 841–851.
le Rousseau, J. H., & de Hoop, M. V., 2001, Scalar generalized–screen algorithms in transversely isotropic media with a vertical symmetry axis, *Geophysics,* **66**, 1538–1550.
Müller, G., Roth, M., & Korn, M., 1992, Seismic–wave traveltimes in random media, *Geophys. J. Int.,* **110**, 29–41.
Müller, T. M., & Shapiro, S. A., 2001, Most probable seismic pulses in single realizations of two– and three–dimensional random media, *Geophys. J. Int.,* **144**, 83–95.
Müller, T. M., & Shapiro, S. A., 2003, Amplitude fluctuations due to diffraction and refraction in anisotropic random media: implications for seismic scattering attenuation estimates, *Geophys. J. Int.,* **155**, 139–148.
Müller, T. M., Shapiro, S. A. & Sick, M. A., 2002, Most probable ballistic waves in random media: a weak–fluctuation approximation and numerical results, *Waves Random Media*, **12**, 223–245.
Musgrave, M. J. P., 1970, *Crystal Acoustics: Introduction to the Study of Elastic Waves and Vibrations in Crystals*, Holden–Day.
Nishizawa, O., Satoh, T., Xinglin, L., & Kuwahara, Y., 1997, Laboratory studies of seismic wave propagation in inhomogeneous media using a laser Doppler vibrometer, *Bull. seism. Soc. Am.,* **87**, 809–823.
Press, W. H., Teukolsky, S. A., Vetterling, W. T. & Flannery, B. P., 1992, *Numerical Recipes in FORTRAN*, Cambridge University Press.
Raymer, D. R., 2000, *The Significance of Salt Anisotropy in Seismic Exploration*, Ph.D. Thesis, School of Earth Sciences, University of Leeds.
Raymer, D. G., Tommasi, A., & Kendall, J–M., 2000, Predicting the seismic implications of salt anisotropy using numerical simulations of halite deformation, *Geophysics,* **65**, 1272–1280.
Sato, H., & Fehler, M. C., 1998, *Seismic Wave Propagation and Scattering in the Heterogeneous Earth*, Springer.
Smith, W. D., 1975, The application of finite element analysis to body wave propagation problems, *Geophys. J. R. astr. Soc.,* **42**, 747–768.
Snieder, R., 1999, Imaging and averaging in complex media, in *Diffuse Waves in Complex Media*, Kluwer Academic Publishers.
Spetzler, J., Sivaji, C., Nishizawa, O., & Fukushima, Y., 2002, A test of ray theory and scattering theory based on laboratory experiment using ultrasonic waves and numerical simulation by finite–difference method, *Geophys. J. Int.,* **148**, 165–178.
Spetzler, J., & Snieder, R., 2001, The formation of caustics in two– and three–dimensional media, *Geophys. J. Int.,* **144**, 175–182.
Tappert, F. D. & Hardin, R. H., 1974, *Computer simulation of long–range ocean acoustic propagation using the parabolic equation method*, in Proc. 8th Intern. Cong. on Acoustics, **2**, Goldcrest, London.
Tatarskii, V. I., 1961, *Wave Propagation in a Turbulent Medium*, McGraw–Hill, New York.
Thomson, C. J., 1999, The 'gap' between seismic ray theory and 'full' wavefield extrapolation, *Geophys. J. Int.,* **137**, 364–380.
Thomson, C. J., 2004, Coherent–state analysis of the seismic head wave problem: an overcomplete representation and its relationship to rays and beams, *Geophys. J. Int.,* **157**, 320–342.
Thomson, C. J., submitted, Accuracy & computational considerations for wide–angle wavefield extrapolators and scattering operators, *Geophys. J. Int.,* , 0–0.
Trorey, A. W., 1970, A simple theory for seismic diffraction, *Geophysics,* **35**, 762–784.
van der Baan, M., 2001, Acoustic wave propagation in one–dimensional random media: the wave localization approach, *Geophys. J. Int.,* **145**, 631–646.
White, B., Nair, B., & Bayliss, A., 1988, Random rays and seismic amplitude anomalies, *Geophysics,* **53**, 903–907.
Wild, A. J., & Hudson, J. A., 1998, A geometrical approach to the elastic complex screen, *J. geophys. Res.,* **103**, 707–725.
Witte, O., Roth, M., & Müller, G., 1996, Ray tracing in random media, *Geophys. J. Int.,* **124**, 159–169.
Woodhouse, J. H., 1974, Surface waves in a laterally varying layered structure, *Geophys. J. R. astr. Soc.,* **37**, 461–490.
Wu, R.–S., 1994, Wide–angle elastic wave one–way propagation in heterogeneous media and an elastic wave complex–screen method, *J. geophys. Res.,* **99**, 751–766.
Wu, R., & Aki, K., 1985, Scattering characteristics of elastic waves by an elastic heterogeneity, *Geophysics,* **50**, 582–595.

Table Captions

Table 1. Mean P– and S–wave velocities of the Gaussian and exponential Cartesian grid random elastic models. Also shown are the approximate ratios of the correlation length a to the spatial pulse–width of the P– and S–waves.

Figure Captions

Figure 1. Two–dimensional section of rays traced through the three–dimensional low–velocity sphere model, where the low–velocity sphere is defined by equation (3.1). At a depth of approximately 700 m, a 'conical–shaped' caustic appears, which would resemble a pencil–point cusp in three–dimensions.

Figure 2. Waveforms of the x_1–component of displacement for an incident plane P–wave in the low–velocity sphere model at x_1–planes of 800, 900 and 1000 m, plotted as profiles along the x_2–axis. The three columns represent the x_3 position on the lateral grid, where $x_3 = 500$ m is the precise midline, $x_3 = 400$ m skirts the side of the sphere and $x_3 = 450$ bisects the other two x_3 positions.

Figure 3. A two–dimensional section of rays traced through the three–dimensional high–velocity sphere model, where the sphere is defined by equation (3.1). The two regions where the rays cross form 'funnel–shaped' caustics, which would resemble rings or circular cusps in three–dimensional space. Also note the geometrical spreading or de–focussing of the rays within the central region. The dotted ellipse represents the region of influence of the ring–cusp diffraction.

Figure 4. Waveforms of the x_1–component of displacement for an incident plane P–wave in the high–velocity sphere model at x_1–planes of 400, 1500 and 2000 m depth, plotted as profiles along the x_2–axis. The three columns represent the x_3 position on the lateral grid, where $x_3 = 1970$ m is just slightly off the midline, $x_3 = 1670$ m skirts the side of the sphere and $x_3 = 1820$ bisects the other two x_3 positions.

Figure 5. Comparison of the x_1–component of displacement for an incident plane P–wave in the high–velocity sphere model for all three x_3 grid locations shown in Figure 4 and depth $x_1 = 2000$ m.

Figure 6. Sketch of 'creeping–wave' diffraction for a plane–wave incident on a smooth isotropic high–velocity spherical anomaly.

Figure 7. Waveforms of the x_1–component of displacement for an incident plane P–wave, plotted as profiles along the x_2–axis. This figure shows the creeping–wave diffraction of a plane P–wave for three high–velocity sphere models, 5%, 6% and 10% velocity perturbation.

Figure 8. (a) The one–dimensional oscillatory velocity field and (b) the focal distance $\breve{x}_1(x_2)$ of a plane–wave propagating in this velocity model. The propagating plane–wave is being focused in regions where the velocity is a minimum and de–focused where the velocity is a maximum. The x_1 distance where a caustic develops is described by the focal distance curve $\breve{x}_1(x_2)$.

Figure 9. Evolution of an incident plane P–wave within the one–dimensional oscillating velocity model defined by equation (3.2). Each panel, after the initial $x_1 = 0$ m panel, represents the evolved wavefield after propagating a distance of roughly one spatial pulse–width. The numbered lines (1 through 6) point to the predicted caustics.

Figure 10. Cartoon of two realizations for the random three–dimensional isotropic, heterogeneous 'mantle in a box' model (modified from Baig et al., 2003).

Figure 11. Waveforms of the x_1–component of displacement for a plane P–wave after propagating 1000 m in the three–dimensional random model with a Gaussian ACF.

Figure 12. Waveforms of the x_2–component of displacement for a plane S–wave after propagating 1000 m in the three–dimensional random model with a Gaussian ACF.

Figure 13. Waveforms of the x_1–component of displacement for a plane P–wave after propagating 1000 m in the three–dimensional random model with an exponential ACF.

Figure 14. Waveforms of the x_2–component of displacement for a plane S–wave after propagating 1000 m in the three–dimensional random model with an exponential ACF.

Figure 15. Comparison of the x_2–component waveforms for a plane S–wave in the Gaussian random media for correlation lengths $a = 500$, 125 and 60 m. The solid line represents the wavefield propagating through the random model and the dashed line the wavefield propagating through the homogeneous model.

Figure 16. Comparison of the x_2–component waveforms for a plane S–wave in the Gaussian random media for correlation lengths $a = 32$, 16 and 4 m.

Figure 17. Cartoon of the three–dimensional random heterogeneous subducted slab model of width w and exponential ACF (modified from Baig et al., 2003).

Figure 18. Waveforms of the x_2–component of displacement for a plane S–wave in the three–dimensional random slab model with correlation length $a = 62.5$ m. In this and the next two figures, the thick horizontal lines represent the lateral spatial extent of the heterogeneous thin slab.

Figure 19. Waveforms of the x_2–component of displacement for a plane S–wave in the three–dimensional random slab model with correlation length $a = 16$ m.

Figure 20. Waveforms of the x_2–component of displacement for a plane S–wave in the three–dimensional random slab model with correlation length $a = 4$ m.

Correlation length a (m)	Gaussian distribution velocity (m/s) Average P–wave	S–wave	Exponential distribution velocity (m/s) Average P–wave	S–wave	Approximate a to spatial pulse–width P–wave	S–wave
500.00	4239.20611	2250.04865	4274.35700	2268.70573	25	50
250.00	4253.54024	2257.65679	4276.19876	2269.68329	12.5	25
125.00	4272.70524	2267.82903	4281.12487	2272.29793	6	12.5
62.500	4287.52834	2275.69671	4288.37607	2276.14665	3	6
31.250	4294.52645	2279.41110	4293.92544	2279.09210	3/2	3
15.625	4296.97958	2280.71315	4296.66976	2280.54871	3/4	3/2
7.8125	4297.90561	2281.20466	4297.74440	2281.11911	2/5	3/4
4.0000	4298.27984	2281.40329	4298.13893	2281.32851	1/5	2/5

Table 1.

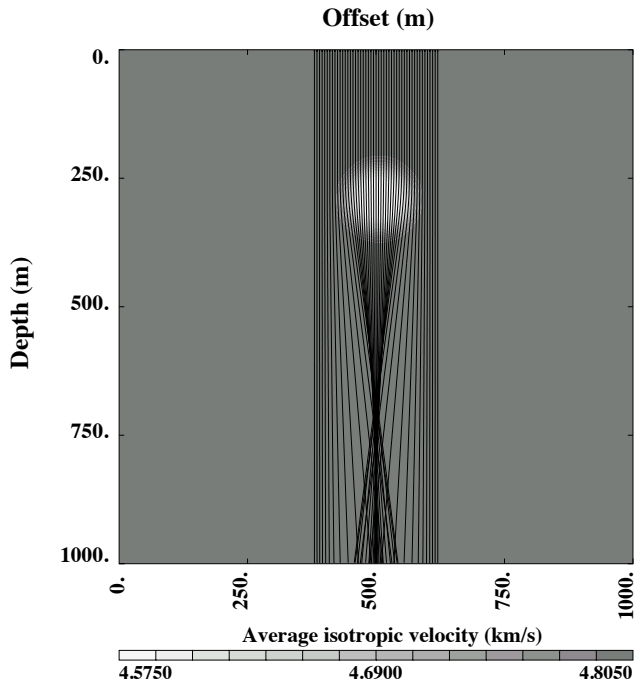

Figure 1.

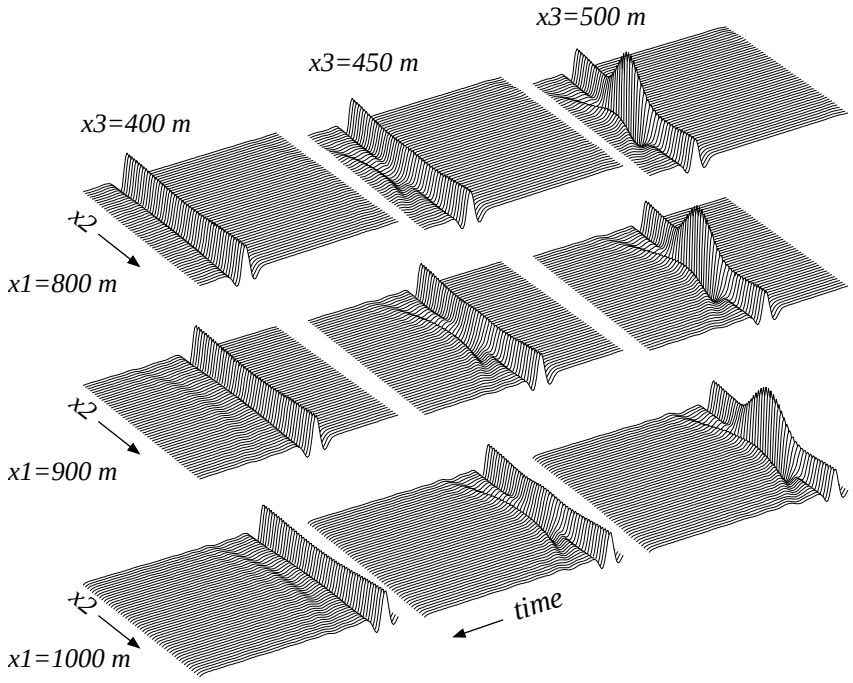

Figure 2.

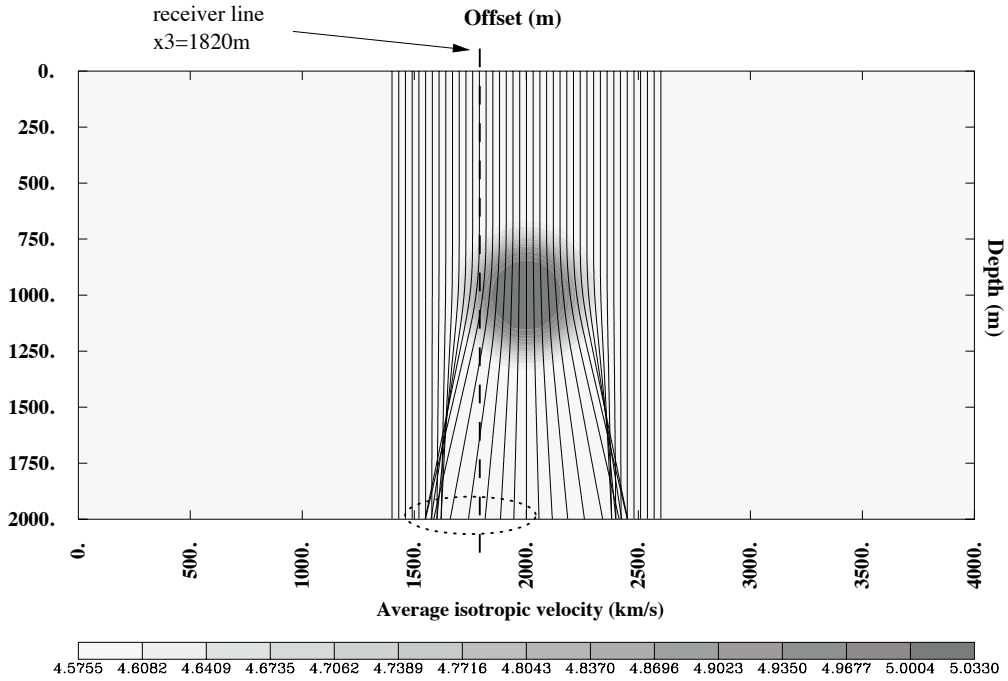

Figure 3.

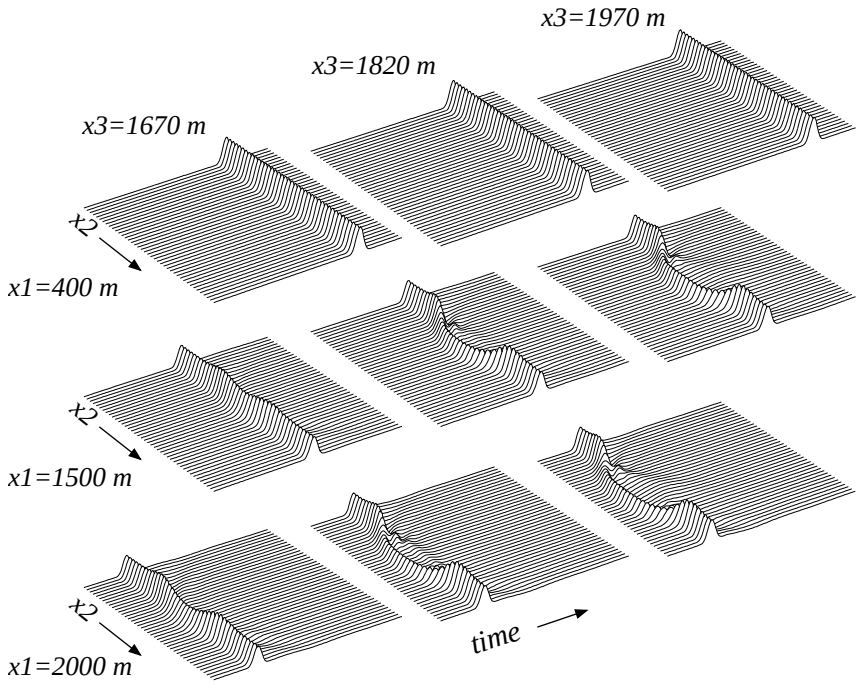

Figure 4.

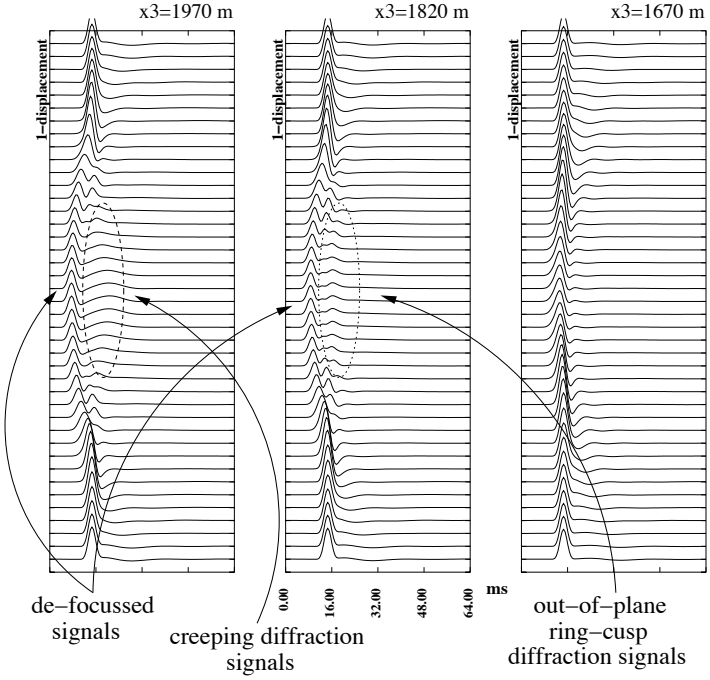

Figure 5.

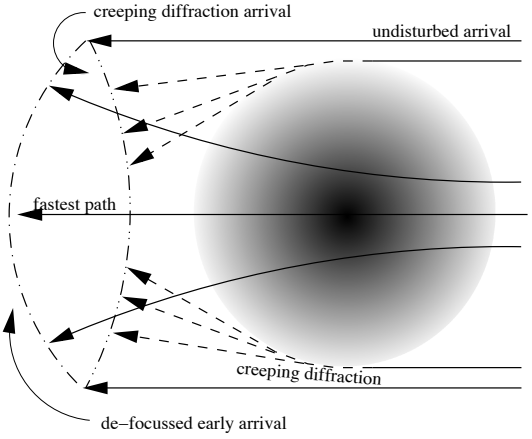

Figure 6.

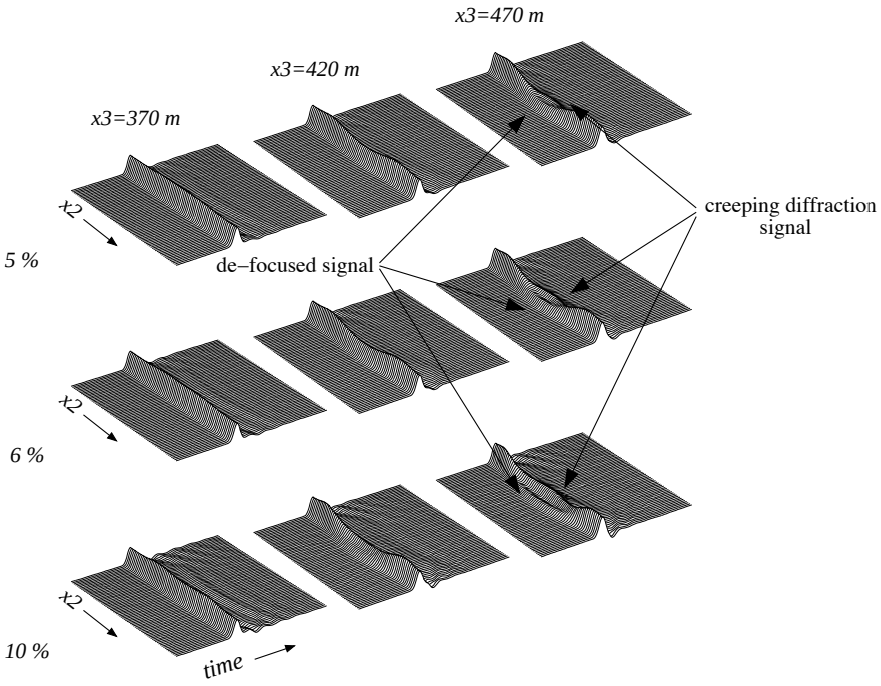

Figure 7.

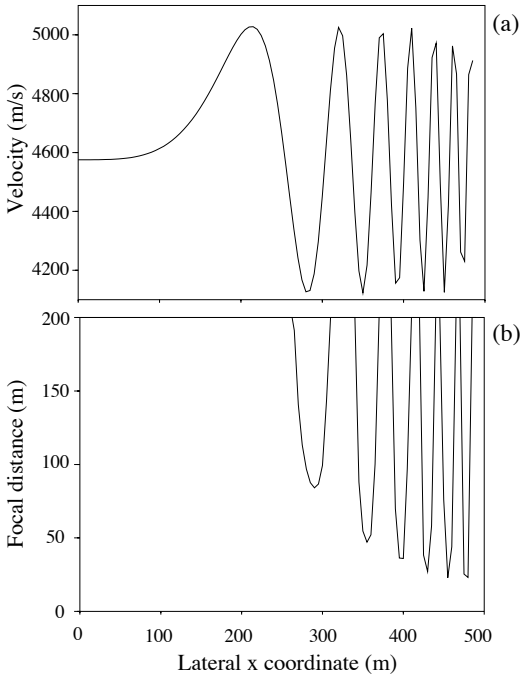

Figure 8.

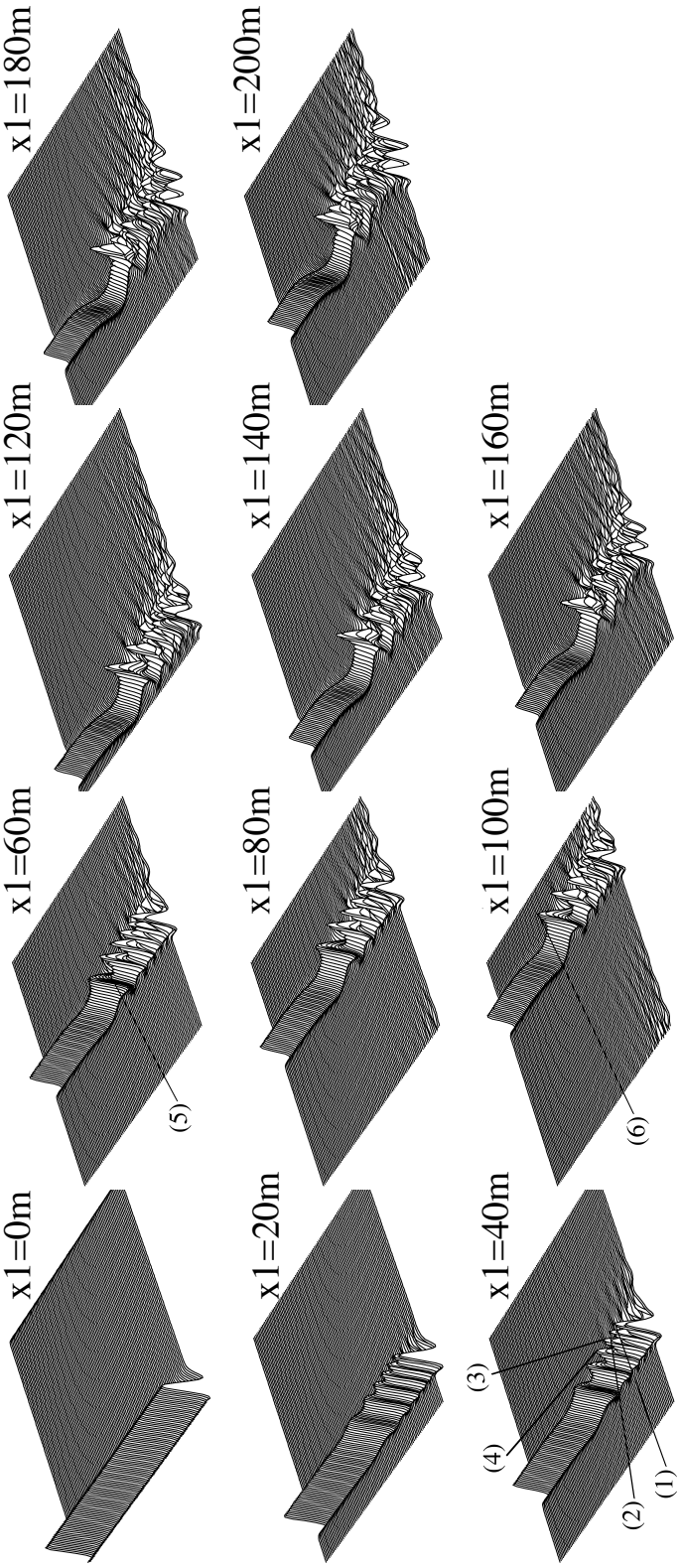
x1=0m
x1=20m
x1=40m
x1=60m
x1=80m
x1=100m
x1=120m
x1=140m
x1=160m
x1=180m
x1=200m
(1)
(2)
(3)
(4)
(5)
(6)

Figure 9.

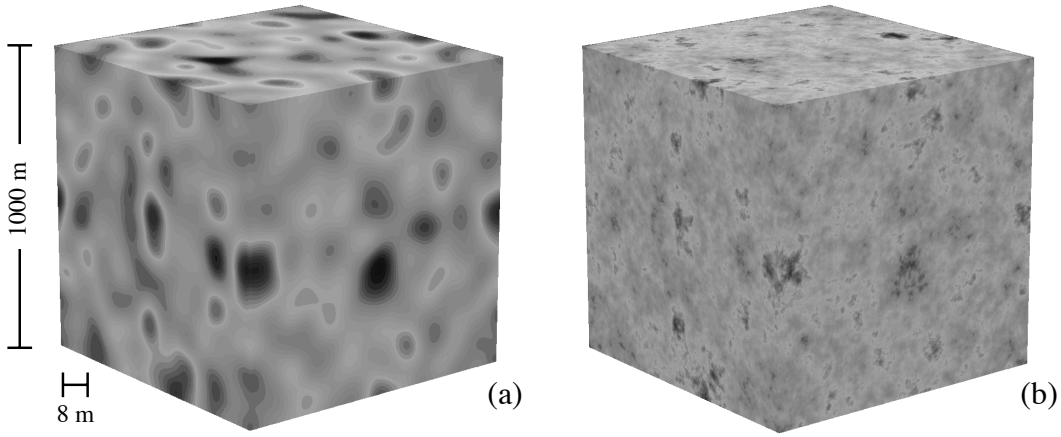

Figure 10.

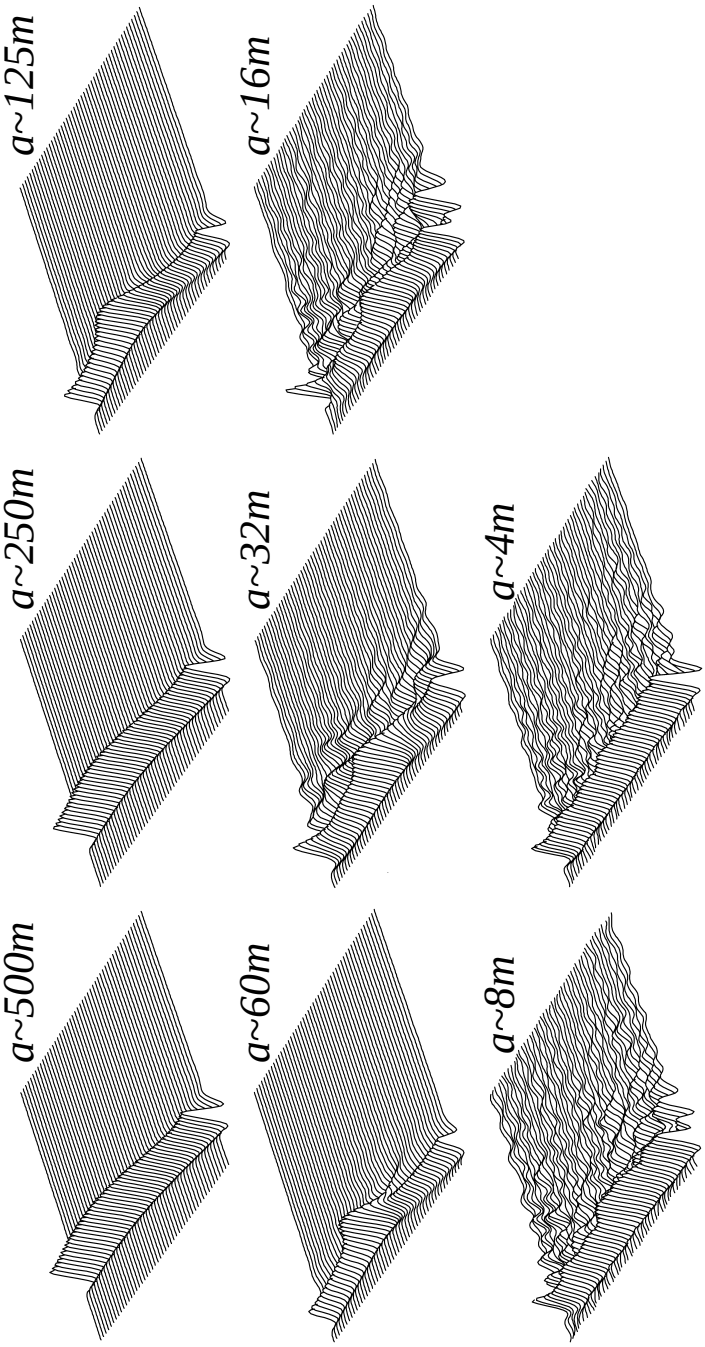

Figure 11.

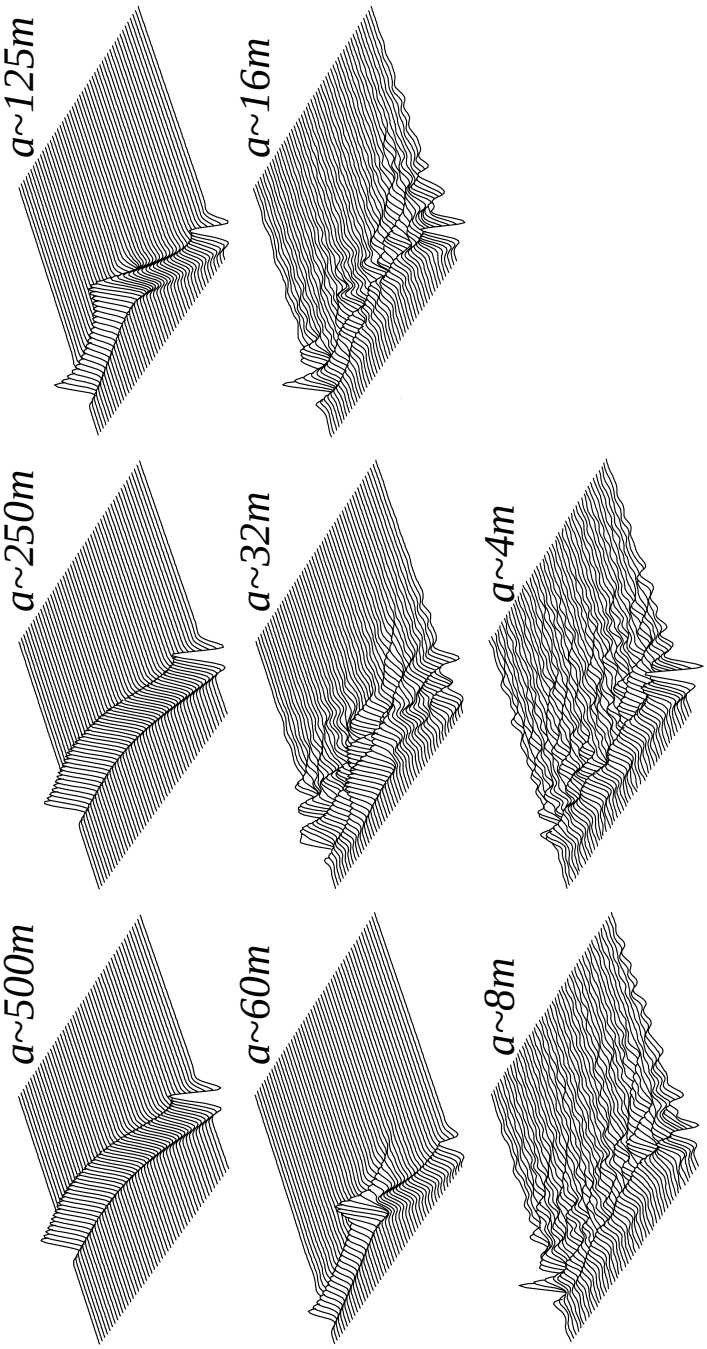

Figure 12.

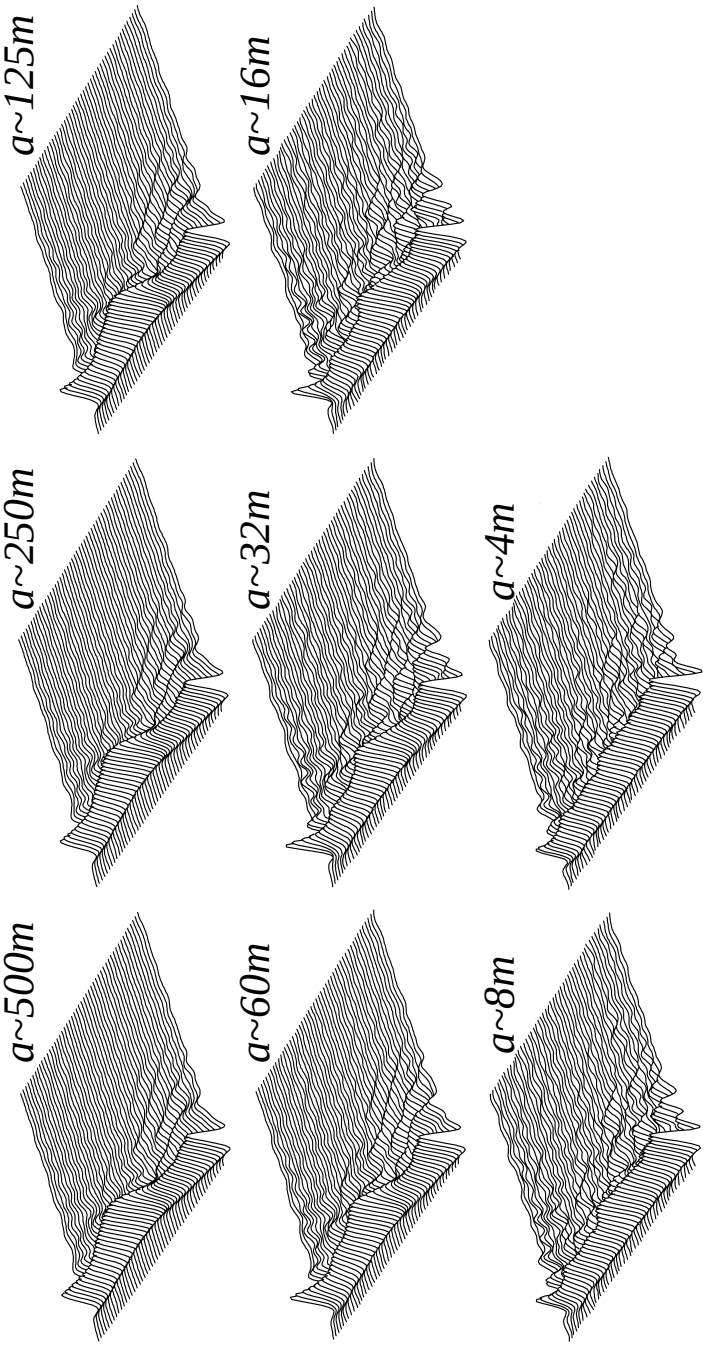

Figure 13.

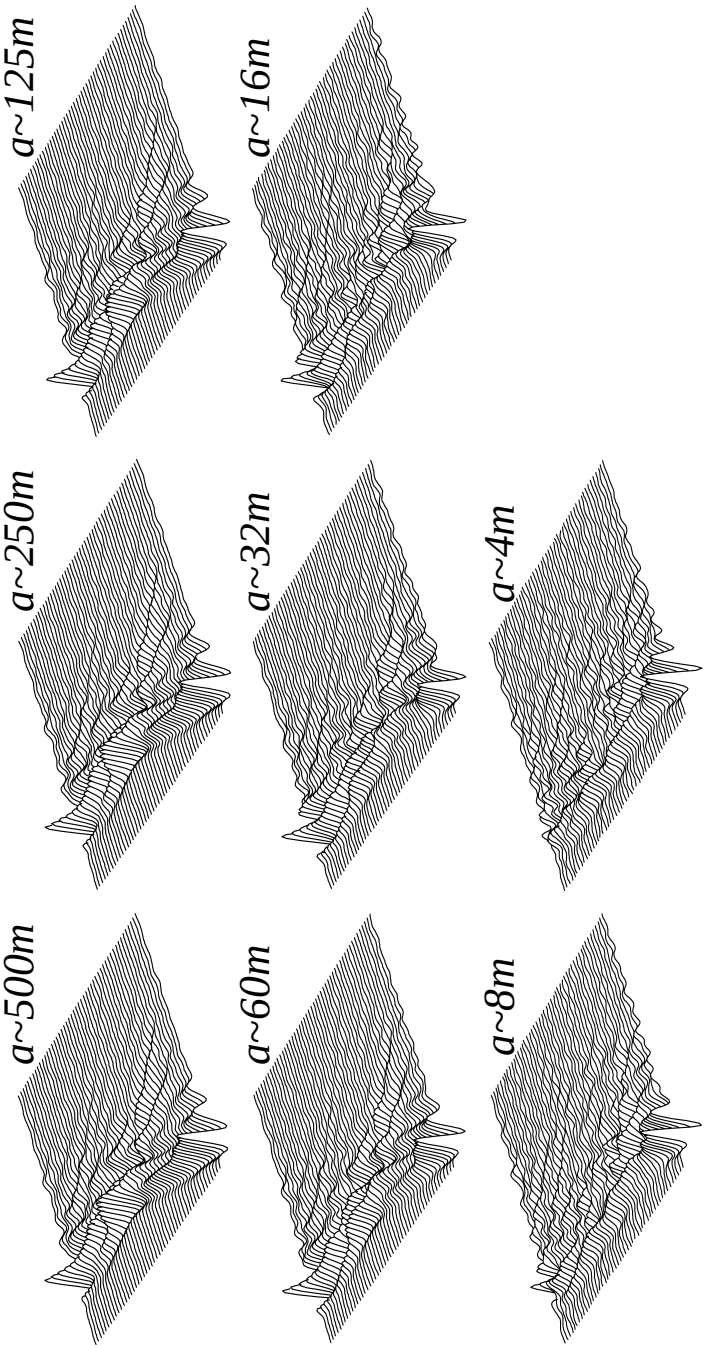

Figure 14.

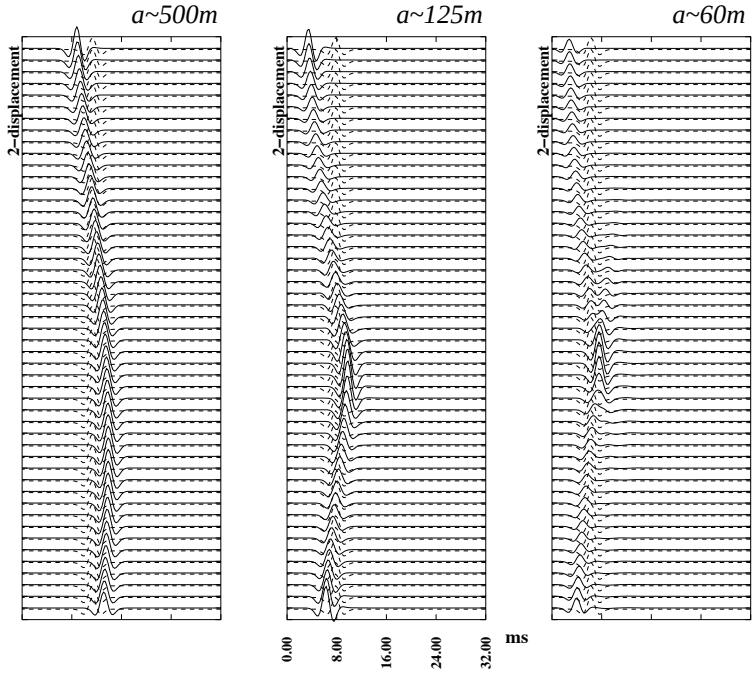

Figure 15.

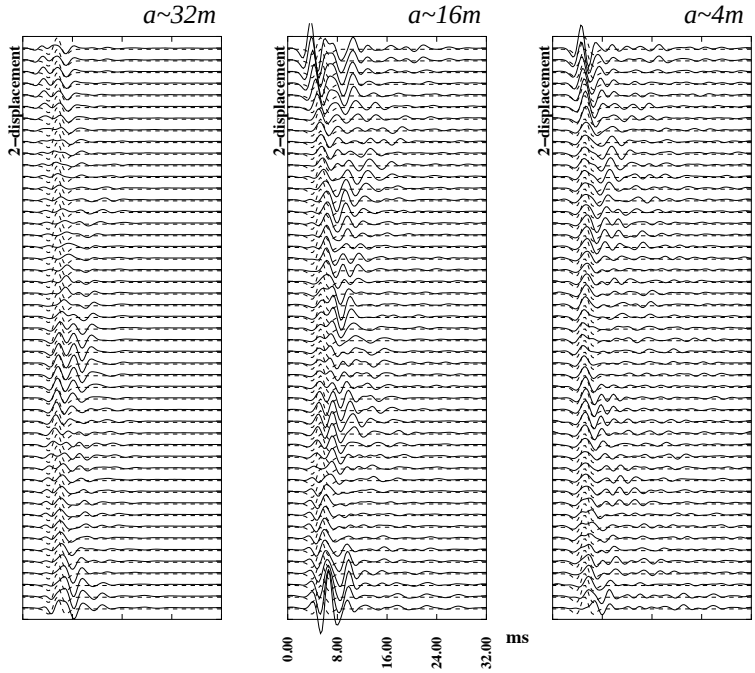

Figure 16.

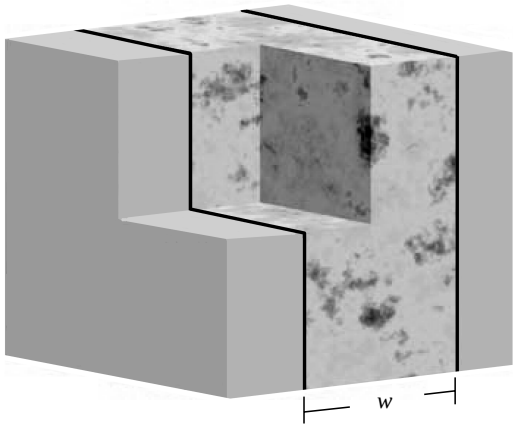

Figure 17.

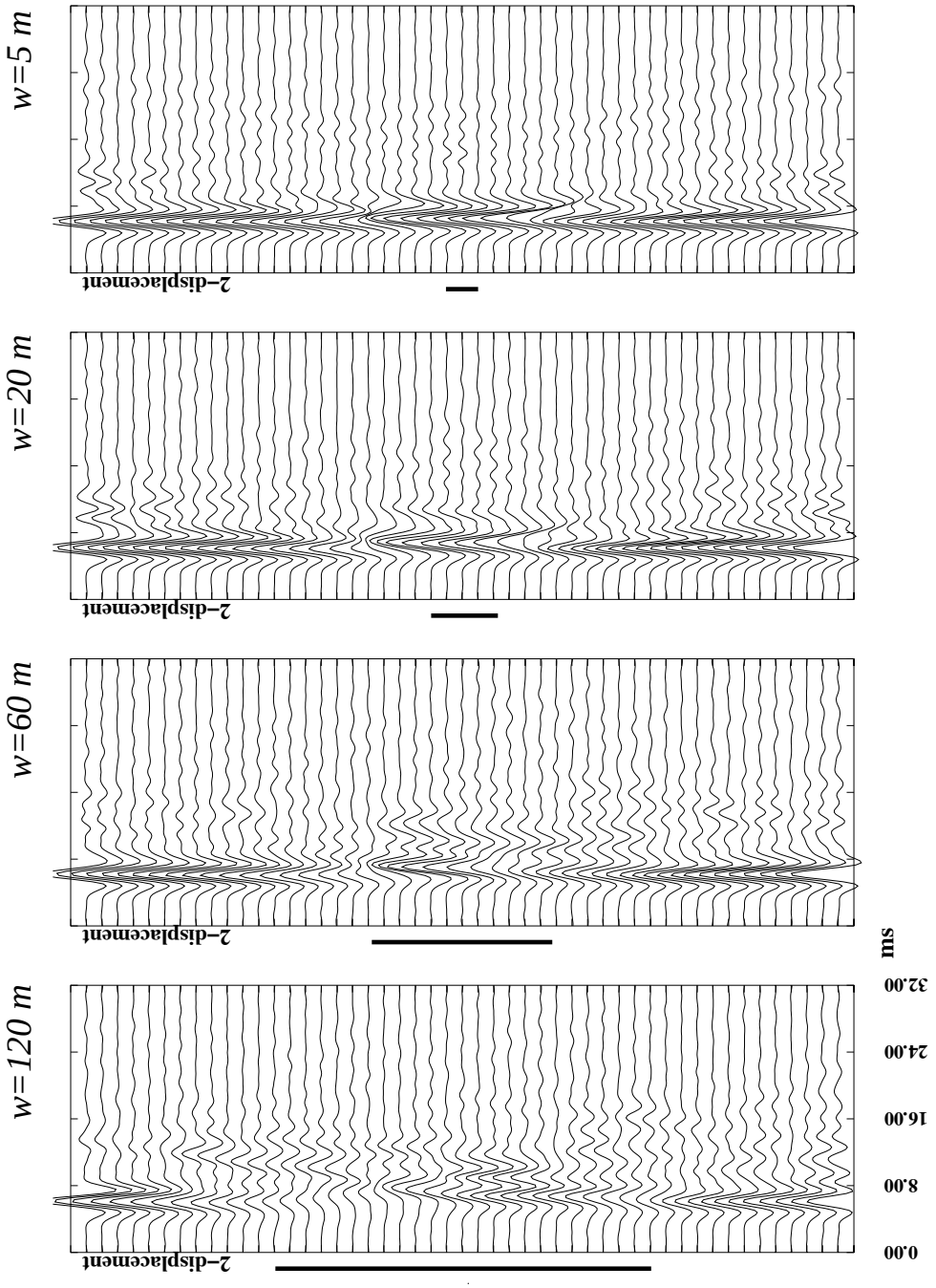

Figure 18.

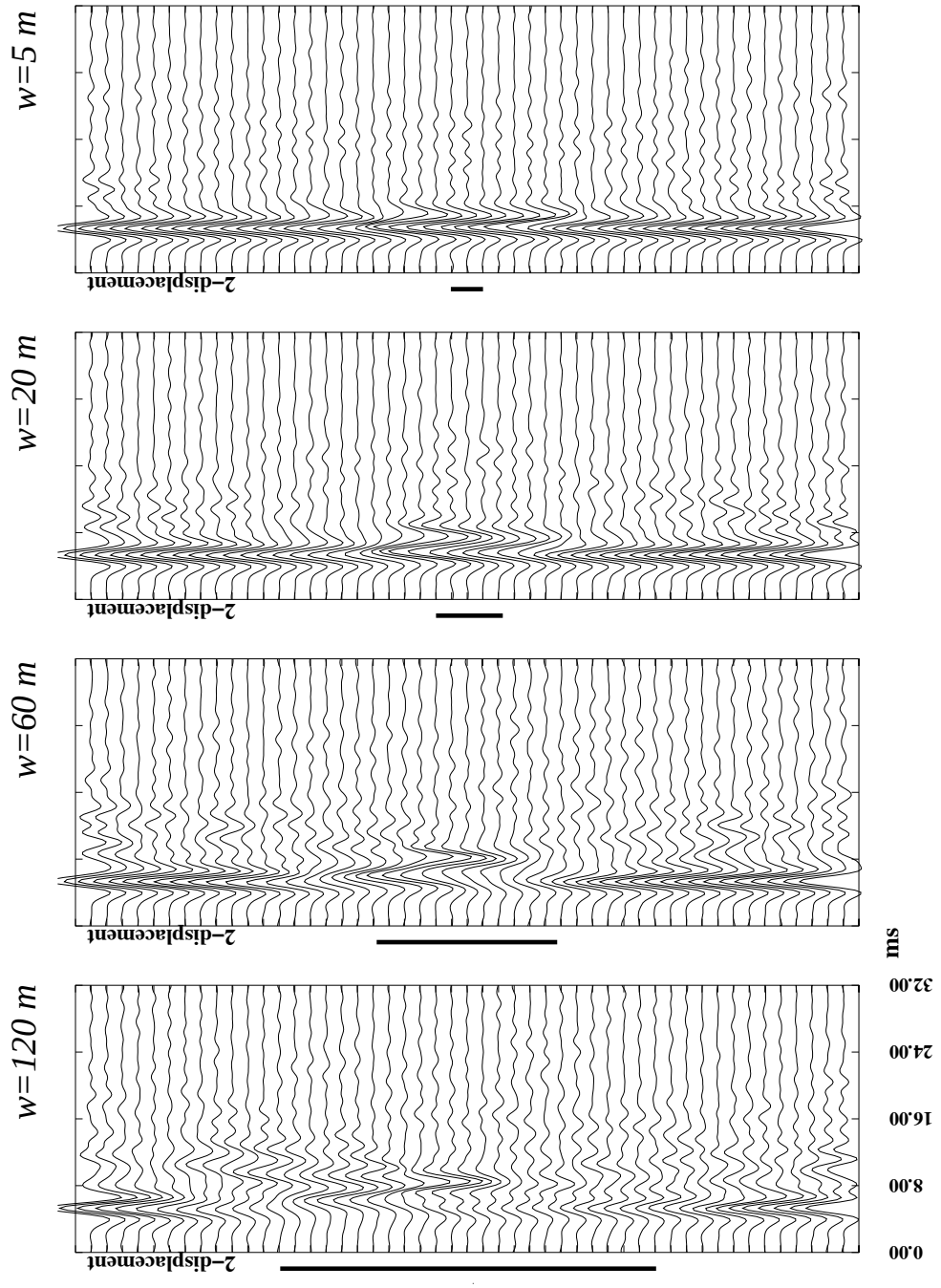

Figure 19.

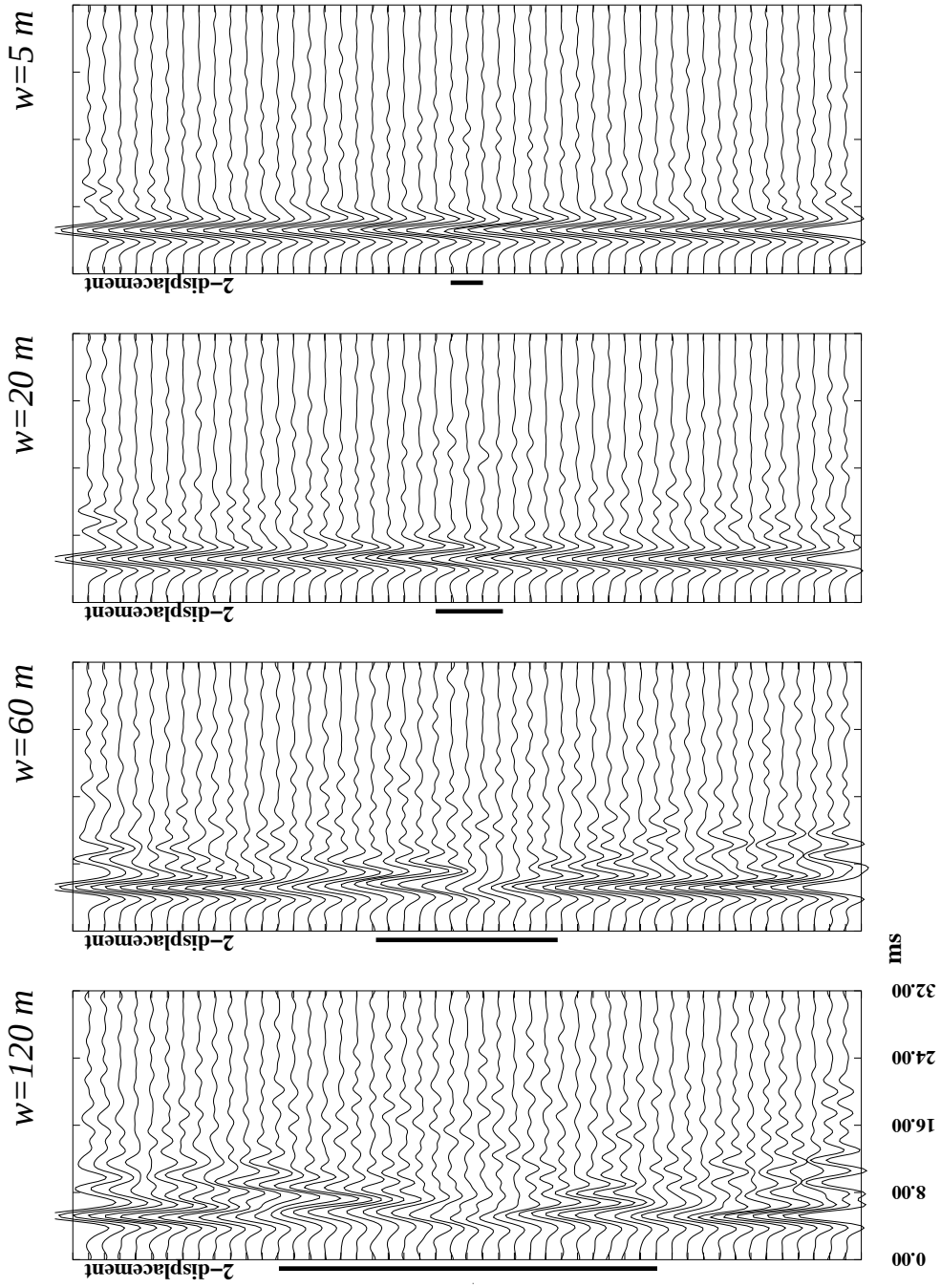

Figure 20.